

Summer Regional Climate Simulations over Tibetan Plateau: From Gray Zone to Convection Permitting Scale

Mengnan Ma

Nanjing University School of Atmospheric Sciences

Tinghai Ou

Department of Earth Sciences, University of Gothenburg

Dongqing Liu

Nanjing Meteorological Bureau

Shuyu Wang

Nanjing University School of Atmospheric Sciences

Juan Fang

Nanjing University School of Atmospheric Sciences

Jiantang Tang (✉ jptang@nju.edu.cn)

School of Atmospheric Sciences, Nanjing University <https://orcid.org/0000-0002-1098-2656>

Research Article

Keywords: Tibetan Plateau, gray zone, convection permitting, spectral nudging, summer precipitation, surface air temperature

Posted Date: January 31st, 2022

DOI: <https://doi.org/10.21203/rs.3.rs-1248790/v1>

License: © ⓘ This work is licensed under a Creative Commons Attribution 4.0 International License.

[Read Full License](#)

Abstract

The Tibetan Plateau (TP) is often referred to as 'the Third Pole' and plays an essential role in influencing the global climate. However, it remains challenging for most global and regional models to realistically simulate the characteristics of long-period climate over the TP. In this study, two Weather Research and Forecasting model (WRF) experiments using the regional climate simulation method of spectral nudging with gray-zone (GZ9) and convection-permitting (CP3) resolution are conducted for summer from 2009 to 2018. The surface air temperature (T2m) and precipitation from the two simulations and the global reanalysis ERA5 are evaluated against in-situ observations. The results show that ERA5 has a general cold bias over southern TP, especially in maximum T2m (Tmax), and wet bias over whole TP. Both experiments can successfully capture the spatial pattern and daily variation of T2m and precipitation, though cold bias for temperature and dry bias for precipitation exist especially over the regions south of 35°N. Compared with ERA5, the added value of the two WRF experiments is mainly reflected in the reduced cold bias especially for Tmax with more improvement found in CP3 and the reduced wet bias. However, the ability of WRF experiments in significantly improving the simulation of precipitation seems limited, which may be related to physical parameterization and lack of representativeness of station observation. Further investigation into surface radiation budget reveals that the underestimation of surface net radiation contributes a lot to the cold bias of T2m over the eastern TP in GZ9 while is improved in CP3 due to more downward solar radiation. Compared with GZ9, CP3 shows larger specific humidity at low-level (mid-high level) coexists with more precipitation (clouds) over the southern TP. This improvement is achieved by better depiction of topographic details and stronger northward water vapor transport (WVT) in CP3, providing more water vapor for precipitation at surface and much wetter condition in the mid-high level.

Key Points

1. Two WRF experiments at gray-zone and convection-permitting scales successfully reproduce the summer climate characteristics over the Tibetan Plateau (TP).
2. Reduced cold bias in convection-permitting simulation is achieved by reducing the underestimation of surface net radiation over the southeastern TP compared with gray-zone simulation.
3. Though simulation with finer resolution has limited ability in reducing the dry bias, more precipitation is still simulated over the southern TP through stronger water vapor transport due to better representation of more realistic topographic features.

1. Introduction

The Tibetan Plateau (TP) extends over the area of 27°-45°N, 70°-105°E, covering a region about a quarter of the size of the Chinese territory (Wu et al. 2007). Surrounded by the Earth's highest mountains, such as the Himalayas, Pamir, Kunlun Shan and others, it is the highest and most extensive plateau in the world

(Kang et al. 2010; Xu et al. 2018; Gu et al. 2020) and has long been known as the roof of the world (Liu and Chen 2000; Qiu et al. 2008; Yao et al. 2019). Mountains in the TP have a strong impact on precipitation distribution, and a knowledge of the characteristics of precipitation is a basic and important requirement for the planning and management of water resources (Xu et al. 2008). Meanwhile, in the summer season, the TP serves as a huge heat source (Zhu et al. 2017), transferring heat from the land surface to the air in the form of sensible heating, latent heat transfer, and effective radiation of the ground (Yeh et al. 1957), with strong surface sensible heating and deep latent heating over the central and eastern regions (Duan et al. 2012), and plays an important role in the onset and maintenance of the Asian summer monsoon (Chen et al. 2017). However, precipitation across the Tibetan Plateau is poorly known compared with many other mountain areas in the world.

The complex climate over the TP is the key component of the regional and global climate system, but the lack of basic observation data makes it difficult to assess the impact that TP has on climate change across scales. Facing the fact that only sparse observation is available from heterogeneously distributed meteorological stations over the TP (Kuang and Jiao 2016; Maussion et al. 2011; Xiao et al. 2016; Li et al. 2018), numerical simulation results have been proven to be a reasonable and reliable complement to enhance the understanding of climate over the TP. Compared to the global climate models (GCMs), regional climate models (RCMs) are able to depict regional heterogeneity and leading to a better understanding of regional to local climate change signals. The main achievements in RCM research are benefited from the increase of simulation length and resolutions (Giorgi et al. 2019). Several studies have shown that added value is obtained by increasing the horizontal resolution of RCMs to capture additional fine-scale weather processes (Jacob et al. 2014; Di Luca et al. 2012; Lucas-Picher et al. 2012). With its complex orography, the TP is very sensitive to the horizontal resolution of RCMs (Gao et al. 2015a, b, 2017b). Gao et al. (2018) found that the WRF model with a resolution of about 30km shows reduced overestimation for extreme precipitation frequency, increased spatial pattern correlations, and more accurate linear trends compared with coarser resolution GCMs and reanalysis over the TP. Xu et al. (2018) showed that the added value of RCM simulation of about 25 km resolution is achieved by affecting the regional air circulation near the ground surface around the edge of the TP, which leads to a redistribution of the transport of atmospheric water vapor.

Convection is considered to be one of the most critical physical processes affecting the occurrence and amount of precipitation (Kukulies et al. 2020; Niu et al. 2020), while cumulus parameterization schemes (CPSs) have been considered to be a primary uncertainty source in precipitation simulations over the TP for coarse resolution (~25km) RCMs (Wang et al. 2021). Attempts have been made to solve the difficulty by further increasing the resolution of RCMs. The gridding space around 10 km is the so-called gray-zone at which resolution the individual convection cells cannot be resolved, but the organized mesoscale convective systems can be explicitly represented (Ou et al. 2020). And when the resolution is reduced to less than 4km, it's widely referred to as convection-permitting scale. With the gray-zone grid spacing, a CPS may or may not be turned on. In Asia, Chen et al. (2018) found that the WRF at the 9km gray-zone resolution without the use of CPS captures the salient features of the Indian summer monsoon as well as the spatial distributions and temporal evolutions of monsoon rainfall. Taraphdar et al. (2021) evaluated

the WRF at the 9km gray-zone resolution over the United Arab Emirates (UAE) and the Middle-East, and found that gray-zone simulations' performance for the synoptic and meso-scale precipitation are comparable to convection-permitting simulations with optimized model physical packages. Ou et al. (2020), based on WRF simulations at gray-zone resolution with different CPSs and a simulation without CPS over the TP, found that the frequencies and initiation timings for short-duration (1–3 h) and long-duration (> 6 h) precipitation events are well captured by the experiment without CPS concerning the precipitation diurnal cycles.

Future directions in RCM research are discussed by Giorgi et al. (2019), with a highlight on the transition to convection-permitting modeling systems. Benefited from the rapid development of high-performance computing resources, convection-permitting models (CPMs) is becoming affordable for climate study, which could explicitly resolve the deep convection (Liang et al. 2004; Dai 2006; Prein et al. 2015; Zhang and Chen 2016), eliminate the biases resulted from the application of CPSs, and narrow the uncertainty from model physics (Weisman et al. 1997; Miura 2007; Schlemmer et al. 2011; Satoh et al. 2014; Ban et al. 2015), especially over regions with prevailing convective activities. The added values, such as improved simulations of the buildup and melting of snowpack as well as improvements of temperature at a height of 2m related to improved representation of orography, have been found in CPM climate simulations. Many studies have also demonstrated the other benefits of using CPMs, including the ability to capture observed precipitation diurnal cycles over subtropics (Fosser et al. 2015; Guo et al. 2019, 2020; Li et al. 2020; Yun et al. 2020), well replicating the spatial distribution of precipitation over complex terrain (Grell et al. 2000; Prein et al. 2013; Rasmussen et al. 2014; Gao et al. 2020), and even capable of representing the spatial-temporal scales and the organization of tropical convection at the nearly global scale (Schiwitalla et al. 2020). However, it is also important to mention that CPM climate simulations are not the cure for all model biases. The largest added value can be found on small spatial and temporal scales (<100 km and subdaily) or in regions with steep orography (Prein et al. 2015) such as TP. Li et al. (2021) demonstrated that CPM is a promising tool for dynamic downscaling over the TP with its higher ability to depict the precipitation frequency and intensity. Zhou et al. (2021) found that CPM outperforms the High Asia Refined regional reanalysis (HAR v2, Wang et al. 2020) for 10-m wind speed and precipitation with obviously reduced wet bias over the TP. Furthermore, process-based analysis methods can reveal deeper insights into the more physically and dynamically consistent atmospheric phenomena in CPM climate simulations. Lin et al. (2018) showed that simulation with finer resolutions (especially 2 km) can diminish the positive precipitation bias over the TP through decreased water vapor transport which is reflected mostly in the weakened wind speed. However, modeling clouds remains a challenge even with CPMs that still requires several parameterizations (shallow convection, microphysics and clouds) that need to be adapted for finer resolutions (Kendon et al. 2021). Thus, to date, one of the main challenges associated with the use of CPMs lies in their heavy computational requirements and demanding output storage sizes (Schär et al. 2020). Another challenge lies in the lack of reliable high temporal and spatial resolution gridded observations, affecting the evaluation of the CPM simulations, and especially the assessment of their added value, often linked with sub-daily time scales and extremes. The above challenges limit the characterizations of the different sources of CPM uncertainties and

hamper their uptake in climate change assessments and impact studies (Lucas-Picher et al. 2021; Prein et al. 2017, 2020).

Both gray-zone and CPM simulations are at their earlier stages in regional climate application, and there are still few studies in intercomparing simulations at gray-zone scale and convection-permitting scale especially over the TP during the past years. A gap exists in understanding the added value from gray-zone to convection-permitting scale, in which a significant increase in computational resources is needed. Furthermore, previous studies with CPM over the TP were mostly limited to short-term simulation. In this study, two types of high-resolution experiments using the WRF model, the gray-zone resolution of 9km with no CPS and the convection-permitting (CP) resolution of 3km, are performed over the TP for the summer of 2009 to 2018. By comparing the two sets of simulation results, we can: (1) evaluate the model's performance with various resolutions in reproducing the spatiotemporal characteristics of surface summer climate over the TP; (2) identify the added value of convection-permitting simulation over complex terrain; and (3) isolate the contribution of the convection-permitting experiments in improving the simulation of regional climate processes.

The article is organized as follows. Section 2 describes the model and experimental design, data and methodology. Section 3 presents the main results as well as the comparison with the observations, including the added value of CPM simulation. Section 4 discusses the possible reasons for explaining the excessive precipitation and higher 2-m air temperature in CPM simulation. Finally, major conclusions are presented in Section 5.

2. Model, Experimental Design And Data

2.1 Model and experimental design

The WRF model version 4.1.1 (Skamarock et al. 2019) used in this study is a nonhydrostatic mesoscale numerical weather prediction system, which is designed to serve both operational forecasting and atmospheric research needs. The WRF model has been widely used for CPM regional climate simulations over Europe (Warrach-Sagi et al. 2013), North America (Gao et al. 2017a; Liu et al. 2017; Sun et al. 2016), Eastern China (Guo et al. 2019, 2020; Yun et al. 2020) and over the TP (Zhou et al. 2021; Gao et al. 2020). The simulation domain in this study is centered at 33°N and 88.5°E, with 1081 (361) grid points in east-west directions and 721 (241) grid points in north-south directions for 3km (9km) resolution, covering the whole TP and the surrounding areas (Figure 1a). Fifty hybrid-sigma levels are defined from surface to model top at 50hPa. The horizontal resolution is set to 9 km for the gray-zone scale simulation (GZ9) and 3 km for the CP scale simulation (CP3) over the TP.

The physical parameterization schemes employed in this research include the Thompson microphysics scheme (Thompson et al. 2008), the Mellor-Yamada Nakanishi Niino 2.5 level TKE scheme (MYNN) planetary boundary layer (PBL) parameterization (Nakanishi and Niino 2006), the RRTMG shortwave and

longwave radiation schemes (Iacono et al. 2008), and the Noah-MP land surface model (Niu et al. 2011). In the two experiments, the CPS is switched off.

Spectral nudging (hereinafter SN, von Storch et al. 2000), which is mostly used in models driven by global analysis (Tang et al. 2010, 2017), has been adopted in CP3 and GZ9. In this study, the nudging wavenumber of 4 is employed in both directions and the nudging coefficient is 3×10^{-4} . Meanwhile, the SN approach is only applied to wind fields above the PBL to allow the development of the mesoscale circulation. Huang et al. (2021) found that model simulations show clear improvements in their representations of downscaled precipitation intensity and its diurnal variations, atmospheric temperature, and water vapor when spectral nudging is applied towards the horizontal wind and geopotential height.

All the experiments are driven by the 4th generation Global Reanalysis data (ERA5) from Europe Centre for Medium-Range Weather Forecasts (ECMWF) (Hersbach et al. 2020) and conducted during the summer season (June, July, and August) from 2009 to 2018. The simulation starts from May 16 and integrates continuously to September 1, with the first 16 days (May 16-31) as the spin-up time.

2.2 Observation data and method

To evaluate the performance of the WRF model in simulating the surface summer climate over the TP, the daily in-situ observation provided by the data service center at China Meteorology Administration (CMA) is used. Only 144 stations over the TP are applied in this study (Figure 1b), which have comparatively more applicable observations of daily surface air temperature (T2m), maximum/minimum surface air temperature (Tmax and Tmin), and precipitation. Most of the meteorological stations are located in the central and eastern part of the TP while few of them are located over the western TP. Therefore, the data from the meteorological stations are not sufficient to fully depict the climate characteristics over the whole TP, especially over the western TP and regions above 4,800 ASL. This is especially true for precipitation which has relatively small spatial scales over the TP (Chen et al. 2016).

In addition, the ERA5 reanalysis dataset is also included in the evaluation of WRF experiments in this study to illustrate the added value of the WRF experiments against ERA5. ERA5 is the fifth generation ECMWF reanalysis for global climate and weather, which combines vast amounts of historical observations into global estimates using advanced modelling and data assimilation systems, and is the latest climate reanalysis produced by ECMWF. It provides 3-hourly and monthly data of various atmospheric, land-surface and oceanic climate variables, and includes information about uncertainties for all the variables at reduced spatial and temporal resolutions. The data covers the Earth on a 30km grid spacing and resolves the atmosphere using 137 levels from the surface up to a height of 80km. Chen and Ji (2019) evaluated the performance of ERA5 over the TP during the period of 1979-2012 and found that ERA5 well reproduces the temporal and spatial variations of surface air temperature and demonstrates overestimation of precipitation in wet season with an average bias of 1.0 mm/d.

The CERES (Clouds and the Earth's Radiant Energy System) (Wielicki et al. 1996) SYN (Synoptic Radiation Fluxes and Clouds) products (Doelling et al. 2013; Rutan et al. 2015) (hereinafter CERES-SYN)

provides a global dataset of radiant fluxes at the surface, top of atmosphere (TOA), and in various atmosphere layers, with the spatial resolution of 1° and the temporal resolution of 1-hourly, 3-hourly, and daily, etc. This dataset is based on measurements from instruments on board the NASA satellites Terra and Aqua which are polar-orbiting satellites and is designed for use in studies of climate and the global or regional surface energy budget. Wang et al. (2021) compared various surface shortwave and longwave radiation products over the three poles and concluded that CERES-SYN has the relatively best accuracy in the Qinghai-Tibet Plateau region. Therefore, the monthly cloud and surface radiation records from CERES-SYN are used for evaluation in this study.

Several statistics are calculated to quantify the accuracy of the WRF simulations, including the correlation coefficient, the uncentered root-mean-square error (RMSE), and the relative bias (RB). The correlation coefficient is used to describe the temporal and spatial similarity between the observations and the simulations. The RMSE can measure the average magnitude of the deviation of a model simulation from the observation, with mean error, correlation coefficient, and standard deviation considered (Taylor et al. 2001). In addition, water vapor transport (WVT) in the model is examined to reveal related physical processes which are supposed to be better represented with finer spatial resolution. WVT at each level is calculated using the following formulas:

$$WVT = v_h \rho r(1)$$

with

$$\rho = \frac{p}{R_d(1 + 0.61r)T}(2)$$

To obtain the total column of WVT, WVT is additionally integrated along the metric z coordinate from surface to the top of the σ levels using the rectangle method as follows:

$$WVT_{col} = \int_{z=z_{sfc}}^{z=z_{top}} v_h \rho r \delta z(3)$$

where ρ is the air density (kgm^{-3}), r the mixing ratio for water vapor ($kgkg^{-1}$), v_h the horizontal wind vector (ms^{-1}), p the pressure (pa), R_d the gas constant, and T the air temperature (K), δz the thickness of each σ level. Detailed description can be found by referring Curio et al. (2015) or Lin et al. (2018).

3. Results From Wrf Simulations At Gray-zone And Convection-permitting Scale

Evaluation of the WRF experiments (CP3 and GZ9) is mainly for the surface summer climate of T2m, Tmax, Tmin, and precipitation. In order to compare with the in-situ observations, the WRF simulation results were interpolated onto the stations when compared with in-situ observations, using the inverse distance weight interpolation method. Due to the elevation difference between WRF grids and station location, lapse rate (LR) is used to bias correct the WRF simulated T2m, Tmax and Tmin as well as that

from ERA5 when evaluating them against in-situ observations (Gao et al. 2015b; Wang et al. 2018; Du et al. 2007; Kattel et al. 2012). According to the spatiotemporal variability of LR proposed by Wang et al. (2018), the mean LRs over the western TP, northeastern TP, and southeastern TP during summer are -4.90 , -4.53 , and -4.03 K/km, respectively, which are consistently lower than the commonly used global mean LR (-6.5 K/km) and are used for bias correction in this study.

3.1 Summer mean surface air temperature and precipitation

Figure 2 shows the 10-year averaged (2009-2018) summer mean daily T2m, Tmax, and Tmin from the in-situ observations, the differences between the WRF simulations and the observations as well as the differences between ERA5 and the observations. The observed T2m decreases from the southeastern TP to the northwestern TP, with the maximum T2m at about 22°C over the eastern TP while the minimum T2m below 8°C over the central TP. Both the WRF experiments can well reproduce the spatial pattern of T2m with the spatial correlation coefficients (SCCs) larger than 0.94, but underestimate the T2m over the regions south of 35°N especially in GZ9. Compared to GZ9, CP3 clearly improves the T2m simulation with lower biases. The simulated distributions of Tmax and Tmin also agree well with the observations, with the SCCs above 0.90 and the RMSEs below 2.7°C . ERA5 shows comparable performance with the WRF experiments in reproducing the spatial pattern of the 10-yr summer mean T2m with SCCs above 0.90. All of the SCCs above are significant at the 0.01 significance level. However, CP3 tends to simulate higher T2m than GZ9 and ERA5 over the TP, thus showing more skillful performance in reducing the cold bias, especially for Tmax which demonstrates the most reduced RMSE compared with GZ9 and ERA5.

The daily temperature range (DTR) is higher over the regions north of 30°N according to the station observations, exceeding 13°C (figure not shown), while the minimum DTR below 10°C is detected over the southeastern TP. Both WRF experiments can well simulate the spatial pattern of DTR with the SCCs about 0.8 and the RMSEs less than 1.5°C . The spatial pattern of DTR in ERA5 is similar to that of WRF experiments, with lower SCC of about 0.68 and larger RMSE of about 2.3°C . Consistent with the underestimation of Tmax, obvious cold bias exists over the southern TP in WRF experiments and ERA5. However, WRF experiments can reduce the RMSE by about 1°C over the southeastern TP compared with ERA5, showing the added value of WRF simulation at both gray zone scale and convection-permitting scale in reducing the cold bias of Tmax, Tmin and DTR.

Figure 3 shows the 10-year averaged summer mean precipitation from the station observations, the WRF simulations, and ERA5 as well as the bias of the WRF simulations and ERA5 against the observations. The observed precipitation decreases from southeast to northwest, with the maximum above 6 mm/day located at the southeastern corner of TP and the minimum less than 1mm/day over the northeast TP. CP3, GZ9 and ERA5 can well capture the spatial distribution of summer mean precipitation, with SCCs larger than 0.7 which are significant at the 0.01 significance level. However, the RMSEs of WRF simulations are about 1.5 mm/day lower than that of ERA5. Meanwhile, the WRF model clearly underestimates summer precipitation over most regions of TP, especially over the southern TP while ERA5 tends to greatly overestimate that with the most severe wet bias which is even larger than 3

mm/day occurring over the southeastern TP. In general, the added value of WRF experiments lies in the reduced bias over the southeastern TP while with the higher spatial resolution, the improvement of dry bias compared with station observation seems to be limited, which may be more related to the physic parameterization in model configuration as well as the lack of representativeness of station observation because they are mostly located at valleys.

The Taylor diagrams are also presented to evaluate the performance of two WRF experiments and ERA5 in simulating the spatial distributions of summer temperature and precipitation (Figure 4) over the TP for each year (2009-2018). For T2m, CP3 slightly outperforms ERA5 but shows relatively more improvement than GZ9 at every single year. For Tmax, GZ9 and ERA5 demonstrates similar performance while CP3 outperforms them with higher SCCs and lower RMSEs at every single year. For Tmin, GZ9, CP3 and ERA5 all have similar performance in reproducing its spatial pattern. Different from T2m for which both WRF's and ERA5's performance shows less annual variability, their performance exhibits more variability in simulating each year's precipitation, especially for ERA5. For the precipitation, the two WRF experiments generally show comparable performances and outperform ERA5 with reduced RMSEs.

In general, compared with ERA5, the added value of WRF experiments is mainly reflected in the reduced cold bias of Tmax, with more improvement found in CP3. Meanwhile, CP3 and GZ9 demonstrate reasonable dry bias while ERA5 shows much wetter bias for precipitation, which may be related to the option of physic parameterization schemes when the CPS is switched off, and the improvement seems to be limited with the finer resolution.

3.2 Daily surface temperature and precipitation

The 10-year averaged (2009-2018) daily variations of the regional mean (over the TP) T2m, Tmax, Tmin, and DTR from the in-situ observations, WRF experiments and ERA5 are shown in Figure 5 (a)-(d). The observed T2m ranges from 12°C to 16°C throughout the summertime, with the maximum T2m in early and middle July. Both WRF experiments and ERA5 can well capture the daily variation of T2m with the temporal correlation coefficients (TCCs) higher than 0.95 and the RMSEs less than 1.1°C. CP3 outperforms GZ9 and ERA5 by reducing the cold bias. With bias correction applied, ERA5 can perform as well as GZ9 in simulating the daily variation of T2m even though the cold bias is significantly reduced in GZ9 compared with ERA5 when no correction is done. The Tmax ranges from 18°C to 24°C based on the observation, and CP3 and GZ9 also well simulate the daily variation with the underestimation of about 1.0°C for CP3 and 2.0°C for GZ9, which is above 3.5°C for ERA5. For Tmin, CP3 can also reduce the RMSE by about 0.6°C compared to GZ9 and about 1.5°C compared to ERA5. The observed DTR varies between 9°C and 15°C, with the minimum DTR occurring in early July. Both WRF experiments reproduce the daily DTR variation with the TCCs larger than 0.91 and the RMSEs less than 1.2°C, and colder bias occurs in late July and early August. CP3 tends to simulate the DTR closer to observation. To conclude, both WRF simulations shows added value for characterizing the spatial pattern and daily variation of extreme temperature (Tmax, Tmin and DTR) with reduced cold bias, and the more improvement can be achieved with finer spatial resolution.

Regarding the daily variation of regional mean precipitation over the TP (Figure 5e), CP3, GZ9 and ERA5 can reproduce the daily variation with the TCCs all about 0.9 and the RMSEs below 0.75 mm/day for WRF experiments and below 2 mm/day for ERA5 when compared with the station observations. It is obvious that ERA5 performs relatively better in capturing the daily variation of summer precipitation, but with severe wet bias that is greatly reduced in WRF simulations.

The spatial distributions of TCCs and RMSEs of T2m, Tmax, and Tmin at each observational station are shown in Figure 6 and Figure 7, respectively. The spatial patterns of TCCs of T2m and Tmax are quite similar in WRF experiments and ERA5, with high TCCs above 0.9 located over the northeastern TP and decrease from north to south. Compared with GZ9, CP3 exhibits higher TCCs of T2m and Tmax, especially over the southern TP. The WRF model has relatively lower performance in simulating variation of Tmin than that of T2m, with the TCCs ranging from 0.5 to 0.8. ERA5 demonstrates similar TCC patterns for T2m and Tmax to those in the WRF experiments, while it produces larger TCCs for Tmin at almost all the stations over the TP. For RMSEs, both experiments and ERA5 show large RMSEs that are above 3.0°C for Tmax over the southern TP, which is greatly reduced in WRF experiments and improves more with higher spatial resolution. CP3 and ERA5 demonstrates smaller RMSEs for T2m compared to GZ9. With the highest resolution, CP3 can reduce RMSEs for T2m, Tmax and Tmin to a large extent. Therefore, it can be concluded that CP3 improves the simulation of T2m with lower RMSEs, especially over the southern TP.

The spatial distribution of TCCs, RMSEs and RBs of the simulated daily precipitation for WRF experiments and ERA5 against station observation is presented in Figure 8. The two experiments show quite similar spatial patterns of TCCs and RMSEs. High TCCs exist over the eastern TP and low RMSEs are located over the central and northern TP. CP3 has slightly increased the TCCs by about 0.1 and reduced the RMSEs by about 0.5 mm/day over the southeastern TP. ERA5 shows higher TCCs that are above 0.7 than WRF experiments. ERA5 shows larger positive RBs at almost all stations over the TP with the largest RBs located over the southeastern TP while WRF experiments have reduced but negative RBs within 30% over the whole TP with the RBs smaller in GZ9, indicating that finer resolution has limited ability in improving the simulation of summer precipitation.

In general, both CP3 and GZ9 show comparable and satisfying performance in reproducing the daily variation of T2m. WRF experiments outperform ERA5 especially in reducing the cold bias for extreme temperatures such as Tmax, Tmin and DTR, and the improvement increases with the higher resolution. Compared to both WRF simulations, ERA5 can better capture the daily variation of precipitation than WRF simulation, but with larger RBs. With finer resolution, the ability of WRF in reducing the dry bias is limited, which may be attributed to the option of physical parameterization schemes.

4. Mechanism

4.1 Surface radiation balance and cloudiness

To investigate the causes of the cold bias of simulated T2m in the WRF, the surface radiation balance is studied based on satellite-derived climate dataset, CERES-SYN. Figure 9 depicts the 10-yr averaged (2009-2018) net radiation (net shortwave radiation and net longwave radiation) at surface from CERES-SYN, GZ9, the difference between GZ9 and CERES-SYN, as well as the difference between GZ9 and CP3. According to the observation, the net radiation at surface is between 100 and 160 W / m^2 over the TP, and the maximum value occurs over the eastern TP. Both WRF experiments successfully reproduce the spatial pattern of the net radiation at surface with an overall slight overestimation over the central TP, while an underestimation of about 24 W / m^2 over the eastern TP is found where the high-value center occurs in CERES-SYN. Therefore, the underestimation of net radiation at surface further contributes a lot to the cold bias of T2m over the eastern TP in GZ9. Instead, the overestimated net radiation in Qaidam Basin leads to the warm bias of T2m in GZ9 to some extent. It can be concluded that the spatial distribution of surface net radiation in GZ9 is closely related to the simulated temperature. Meanwhile, for CP3, even though the obvious underestimation of net radiation over the eastern TP still exists (figure not shown), it has been improved a lot with more simulated net radiation than GZ9 which is up to 10 W / m^2 over the eastern TP and the southeastern TP, which helps explaining the reduced cold bias over the southeastern TP in CP3. In addition, over the southern TP where the precipitation is more abundant, the factors that may influence the temperature are also believed to be more complex. Thus, in CP3, the more simulated precipitation (which is emphatically analyzed in the next section) which will reduce the temperature may also participates in forming the spatial pattern of T2m.

Through the separate comparison of shortwave radiation and longwave radiation at surface in CP3 and GZ9, it can be found that the reduced underestimation of surface net radiation in CP3 comes mainly from the increase in downward shortwave radiation. Thus, the cloud cover at 500-300hPa, which is considered to be the low level of atmosphere over the TP and plays a crucial role in modulating the radiation budget, is examined to tell the reason why there is more downward solar radiation in CP3. Figure 10 presents the 10-yr averaged summer mean spatial distribution of cloud cover at 500-300hPa from CERES-SYN, GZ9, the difference between GZ9 and CERES-SYN, as well as the difference between GZ9 and CP3. Though the spatial pattern of low-level cloud cover is well simulated by the WRF model with the SCC of about 0.71 for GZ9 and 0.76 for CP3, an overall underestimation of low-level cloud cover is detected in both experiments, which is related to the underestimated downward solar radiation over 40 W / m^2 compared with CERES-SYN (figure not shown). Even so, the intercomparison between two WRF experiments reveals that there are fewer low-level clouds in CP3 over the TP, reflecting less shortwave radiation back and thus receiving more energy. The daytime cloud cover at 500-300hPa that plays a more crucial role in modulating the downward shortwave radiation is additionally examined (figure not shown) and results show that CP3 also simulates fewer clouds of about 8%, especially over the southeastern TP, which matches much well with the more downward shortwave radiation than GZ9.

Meanwhile, the comparison of cloud cover above 300hPa which can be treated as mid-high level over the TP between WRF simulation and satellite-derived observation is also provided (Figure 11). Obviously, there are consistently less clouds above 300hPa but more clouds at 500-300hPa in the observation and

WRF experiments. The WRF model also successfully captures the spatial pattern of cloud cover above 300hPa with the SCC of about 0.81 for GZ9 and 0.90 for CP3. Similar to the situation of low-level cloud cover, both model results underestimate that especially over the central TP and eastern TP with the underestimation above 10%, whereas more clouds are simulated by CP3 over the central TP and eastern TP, which is contrary to the results of low-level clouds. Even so, CP3 still simulates overall less total cloud cover than GZ9 (figure not shown) which is consistent with the spatial pattern in the low-level and helps receiving more shortwave radiation and raising the T2m.

4.2 Water vapor

Considering that few stations are located at mountain peaks and ridges, the evaluation of precipitation above is limited to valleys as well. In order to get a comprehensive understanding of the simulation difference of precipitation between CP3 and GZ9, the simulated precipitation in both experiments are compared directly without interpolated to station sites to avoid information loss. Figure 12 provides the 10-yr averaged simulated summer precipitation of GZ9, CP3 and the difference between them at WRF grids. The results show that summer precipitation mainly occurs over the southeastern TP and along the south slope of TP. Generally, CP3 tends to simulate more precipitation of about 1 mm/day over the southern TP than GZ9. Meanwhile, larger specific humidity is also found at 500hPa over the southern TP in CP3 than GZ9 (Figure 13). In addition, larger specific humidity is also found in CP3 at 300hPa and 200hPa (Figure 14 and Figure 15), which is also related to more clouds above 300hPa in CP3. The fact that, over the southern TP, there are larger specific humidity at low-level which is related to more precipitation and consistently larger specific humidity at mid-high level which is related to more clouds especially over the southern TP, indicates that more water vapor is simulated in CP3 than in GZ9 and raises the question to be answered that why CP3 tends to produce more water vapor over the southern TP.

Figure 16 (a) and (b) show the topography of 26.5-29°N, 85.5-90°E (framed with black lines in Figure 15 (b), (c) and (d)) in CP3 and GZ9 where the very complex terrain is of particular concern. The steep terrain here is generally considered to be a barrier for water vapor transport to the TP, however, there are many meridional canyons in this region that may function as vapor channels (Bookhagen and Burbank 2010). Intercomparison of the two WRF experiments' performance in depicting the topography shows that GZ9 heavily smooths the topography while more detailed characterization of the steep terrain is represented in CP3. Moreover, the fact that CP3 outperforms GZ9 in realistically distinguishing pathways and barriers for vapor transport, reproducing the possible meridional canyons and depicting the channeling effect of valleys is supported by the validation that there is stronger WVT from the south and into the TP as is shown in Figure 16 (c) and (d). It is obvious that the northward WVT is more active in CP3 and provides the necessary water vapor for the formation of precipitation and clouds. This improvement in CP3 definitely benefits from the better representation of topography, confirming the resolution dependency of WVT. Therefore, finer model resolution becomes critical to not only realistically represent more mesoscale features but also simulate the physical processes such as WVT over the complex terrain like TP.

To conclude, a sufficient model resolution is proved to be beneficial to capture more terrain features over the southern TP while coarse resolution is challenged with more information loss. The topographical

barrier and channeling effects, which are better simulated in CP3, are reflected in the more realistically simulated meridional canyons and stronger northward WVT over the southern TP. Consequently, in the low level, the more abundant water vapor is strongly influenced by the steep terrain and tends to produce more precipitation over the southern TP in CP3, which is also validated by the direct comparison of precipitation as well as the specific humidity at 500hPa. Whereas, in the mid-high level, the modulation effect of steep terrain weakens a lot and the surplus water vapor is able to spread farther over the whole TP, which favors the formation of more cloud in the most areas of TP. This deduction is also validated by the spatial pattern of specific humidity at 300 and 200hPa, explaining more cloud cover above 300hPa in CP3.

5. Conclusions

Two WRF experiments with the regional climate simulation schemes of spectral nudging at gray-zone and convection-permitting resolution are performed over the TP from 2009 to 2018. The surface air temperature and the precipitation are evaluated based on the in-situ observations, and possible mechanisms are discussed.

Both WRF experiments successfully capture the spatial patterns and the daily variations of T2m, Tmax, and Tmin, with the SCCs and TCCs higher than 0.9. A generally cold bias is found, especially over the regions south of 35°N for Tmax. Compared with GZ9, CP3 shows more skillful performance in reducing the RMSEs over the southern TP for T2m, Tmax, and Tmin. Meanwhile, CP3 has improved TCCs and reduced RMSEs over the southern TP for T2m and Tmax. The DTR is underestimated by about 1°C spatially and temporally in both experiments, with reduced cold bias especially over the southeastern TP in CP3. ERA5 shows comparable performance with the WRF experiments in reproducing the spatial pattern and daily variation of temperature, with greater underestimation and larger RMSEs than WRF experiments. Therefore, compared with ERA5, the added value of WRF simulation at both gray zone scale and convection-permitting scale is mainly reflected in the reduction of cold bias, and more improvement can be achieved with finer spatial resolution especially over the southern TP. Further investigation into the surface radiation balance reveals that the underestimation of surface net radiation contributes a lot to the cold bias of surface air temperature over the eastern TP while the overestimation of net radiation in Qaidam Basin leads to the warm bias of surface air temperature in GZ9. Meanwhile, for CP3, the improved underestimation of net radiation which mainly comes from the more downward solar radiation greatly results in the reduced cold bias of surface air temperature.

The spatial pattern and daily variation of summer precipitation are also reasonably reproduced in both WRF experiments, with the SCCs larger than 0.7 and the TCCs larger than 0.9. The WRF model clearly underestimates summer precipitation especially over the southern TP while ERA5 tends to greatly overestimate that. Compared with ERA5, the added value of WRF experiments is reflected in the reduced bias over the southeastern TP while with the higher spatial resolution, the improvement of dry bias compared with station observation seems to be limited, which may be related to the physic parameterization in model configuration as well as the limited representativeness of station locations.

Intercomparison between CP3 and GZ9 shows that larger specific humidity at low-level coexists with more precipitation and larger specific humidity at mid-high level coexists with more clouds consistently especially over the southern TP. Further, it is proved that CP3 outperforms GZ9 in characterizing more detailed terrain features and thus more realistically simulating the possible meridional canyons for WVT. The stronger WVT in CP3 provides sufficient water vapor for precipitation in the low-level, which is mostly limited over the southern TP under the influence of steep terrain, while spread farther in the mid-high level, leading to the wetter condition over most areas of TP.

Based on the analysis of surface air temperature and precipitation over the TP from 2009 to 2018, WRF experiments at gray-zone and convection-permitting scales generally show comparable performance in successfully reproducing the spatial and temporal variation of multi-year summer climate. A higher horizontal resolution, therefore, has complex effects on the results of simulations. For example, our results show that even though CP3 can reduce the RMSEs for temperature, its ability in significantly improving the simulation of precipitation is limited based on available observations with sufficient accuracy. In addition, for the purpose of saving computation costs, experiments with gray-zone resolution are also a better choice especially for simulating long-period climate over the TP. Future studies in this area should include establishing more reliable high temporal and spatial resolution gridded observations to promote the evaluation of the convection-permitting simulations, further looking for more advantages in experiments with convection-permitting resolution and making more improvements to experiments with gray-zone resolution to make them better utilized in the field of climate studies.

Declarations

Acknowledgments:

The research is supported by the Second Tibetan Plateau Scientific Expedition and Research Program (STEP, Grant No.2019QZKK0206), National Key Research and Development Program of China (2018YFA0606003) and the National Natural Science Foundation of China (41875124) as well as the Swedish Foundation for International Cooperation in Research and Higher Education (CH2019-8377).

Authors' contributions:

All authors contributed to the study conception and design. Material preparation, data collection and analysis were performed by Mengnan Ma, Dongqing Liu and Juan Fang. Tinghai Ou, Shuyu Wang and Jianping Tang helped perform the analysis with constructive discussions. The first draft of the manuscript was written by Mengnan Ma and all authors commented on previous versions of the manuscript. All authors read and approved the final manuscript.

Funding:

This work was supported by the Second Tibetan Plateau Scientific Expedition and Research Program (STEP, Grant No.2019QZKK0206), National Key Research and Development Program of China

(2018YFA0606003) and the National Natural Science Foundation of China (41875124) as well as the Swedish Foundation for International Cooperation in Research and Higher Education (CH2019-8377).

Availability of data and material

The station observations used in this work are available at: <http://data.cma.cn/en>.

The ERA5 dataset used in this work is available at:

<https://www.ecmwf.int/en/forecasts/datasets/reanalysis-datasets/era5>

The CERES-SYN dataset used in this work is available at: <https://ceres.larc.nasa.gov/data/>

Code availability

The analysis code is available on request from the corresponding author.

1. Conflicts of interest

The authors have no conflicts of interest to declare that are relevant to the content of this article.

2. Consent to participate

Written informed consent was obtained from all participants.

3. Consent for publication

Written informed consent for publication was obtained from all participants.

References

1. Ban N, Schmidli J, Schär C (2015) Heavy precipitation in a changing climate: Does short-term summer precipitation increase faster? *Geophys Res Lett* 42(4):1165–1172. <https://doi.org/10.1002/2014gl062588>
2. Bookhagen B, Burbank DW (2010) Toward a complete Himalayan hydrological budget: Spatiotemporal distribution of snowmelt and rainfall and their impact on river discharge. *J Phys Res* 115(F3). <https://doi.org/10.1029/2009jf001426>
3. Chen D, Tian Y, Yao T, Ou T (2016), Aug 24 Satellite measurements reveal strong anisotropy in spatial coherence of climate variations over the Tibet Plateau. *Sci Rep*, 6, 30304. <https://doi.org/10.1038/srep30304>
4. Chen X, Liu Y, Wu G (2017) Understanding the surface temperature cold bias in CMIP5 AGCMs over the Tibetan Plateau. *Adv Atmos Sci* 34(12):1447–1460. <https://doi.org/10.1007/s00376-017-6326-9>
5. Chen X, Pauluis OM, Zhang F (2018) Regional simulation of Indian summer monsoon intraseasonal oscillations at gray-zone resolution. *Atmos Chem Phys* 18(2):1003–1022.

<https://doi.org/10.5194/acp-18-1003-2018>

6. Chen Y, Ji D (2019) Evaluation of ERA5 atmospheric reanalysis datasets for surface climatology over the Tibetan Plateau. AGU Fall Meeting Abstracts
7. Curio J, Maussion F, Scherer D (2015) A 12-year high-resolution climatology of atmospheric water transport over the Tibetan Plateau. *Earth Sys Dyn* 6(1):109–124. <https://doi.org/10.5194/esd-6-109-2015>
8. Dai A (2006) Precipitation characteristics in eighteen coupled climate models. *J Clim* 19(18):4605–4630. <https://doi.org/10.1175/JCLI3884.1>
9. Di Luca A, de Elía R, Laprise R (2011) Potential for added value in precipitation simulated by high-resolution nested Regional Climate Models and observations. *Clim Dyn* 38(5–6):1229–1247. <https://doi.org/10.1007/s00382-011-1068-3>
10. Doelling DR, Loeb NG, Keyes DF, Nordeen ML, Morstad D, Nguyen C, Wielicki BA, Young DF, Sun M (2013) Geostationary enhanced temporal interpolation for CERES flux products. *J Atmos Ocean Technol* 30(6):1072–1090. <https://doi.org/10.1175/JTECH-D-12-00136.1>
11. Du M, Kawashima S, Yonemura S, Yamada T, Zhang X, Liu J, Li Y, Gu S, Tang Y (2007) Temperature distribution in the high mountain regions on the Tibetan Plateau—Measurement and simulation. Proc. MODSIM 2007 International Congress on Modelling and Simulation. Modelling and Simulation Society of Australia and New Zealand
12. Duan A, Wu G, Liu Y, Ma Y, Zhao P (2012) Weather and climate effects of the Tibetan Plateau. *Adv Atmos Sci* 29(5):978–992. <https://doi.org/10.1007/s00376-012-1220-y>
13. Fosser G, Khodayar S, Berg P (2015) Benefit of convection permitting climate model simulations in the representation of convective precipitation. *Clim Dyn* 44(1–2):45–60. <https://doi.org/10.1007/s00382-014-2242-1>
14. Gao Y, Chen F, Jiang Y (2020) Evaluation of a Convection-Permitting Modeling of Precipitation over the Tibetan Plateau and Its Influences on the Simulation of Snow-Cover Fraction. *J Hydrometeorol* 21(7):1531–1548. <https://doi.org/10.1175/jhm-d-19-0277.1>
15. Gao Y, Leung LR, Zhang Y, Cuo L (2015a) Changes in Moisture Flux over the Tibetan Plateau during 1979–2011: Insights from a High-Resolution Simulation. *J Clim* 28(10):4185–4197. <https://doi.org/10.1175/jcli-d-14-00581.1>
16. Gao Y, Leung LR, Zhao C, Hagos S (2017a) Sensitivity of U.S. summer precipitation to model resolution and convective parameterizations across gray zone resolutions. *Journal of Geophysical Research: Atmospheres* 122(5):2714–2733. <https://doi.org/10.1002/2016jd025896>
17. Gao Y, Xiao L, Chen D, Chen F, Xu J, Xu Y (2017b) Quantification of the relative role of land-surface processes and large-scale forcing in dynamic downscaling over the Tibetan Plateau. *Clim Dyn* 48(5–6):1705–1721. <https://doi.org/10.1007/s00382-016-3168-6>
18. Gao Y, Xiao L, Chen D, Xu J, Zhang H (2018) Comparison between past and future extreme precipitations simulated by global and regional climate models over the Tibetan Plateau. *Int J Climatol* 38(3):1285–1297. <https://doi.org/10.1002/joc.5243>

19. Gao Y, Xu J, Chen D (2015b) Evaluation of WRF mesoscale climate simulations over the Tibetan Plateau during 1979–2011. *J Clim* 28(7):2823–2841. <https://doi.org/10.1175/jcli-d-14-00300.1>
20. Giorgi F (2019) Thirty Years of Regional Climate Modeling: Where Are We and Where Are We Going next? *Journal of Geophysical Research: Atmospheres*. <https://doi.org/10.1029/2018jd030094>
21. Grell GA, Schade L, Knoche R, Pfeiffer A, Egger J (2000) Nonhydrostatic climate simulations of precipitation over complex terrain. *Journal of Geophysical Research: Atmospheres* 105(D24):29595–29608. <https://doi.org/10.1029/2000jd900445>
22. Gu H, Yu Z, Peltier WR, Wang X (2020) Sensitivity studies and comprehensive evaluation of RegCM4.6.1 high-resolution climate simulations over the Tibetan Plateau. *Clim Dyn* 54(7–8):3781–3801. <https://doi.org/10.1007/s00382-020-05205-6>
23. Guo Z, Fang J, Sun X, Tang J, Yang Y, Tang J (2020) Decadal long convection-permitting regional climate simulations over eastern China: evaluation of diurnal cycle of precipitation. *Clim Dyn* 54(3):1329–1349. <https://doi.org/10.1007/s00382-019-05061-z>
24. Guo Z, Fang J, Sun X, Yang Y, Tang J (2019) Sensitivity of Summer Precipitation Simulation to Microphysics Parameterization Over Eastern China: Convection-Permitting Regional Climate Simulation. *Journal of Geophysical Research: Atmospheres* 124(16):9183–9204. <https://doi.org/10.1029/2019jd030295>
25. Hersbach H, Bell B, Berrisford P, Hirahara S, Horányi A, Muñoz-Sabater J, Nicolas J, Peubey C, Radu R, Schepers D, Simmons A, Soci C, Abdalla S, Abellan X, Balsamo G, Bechtold P, Biavati G, Bidlot J, Bonavita M, Chiara G, Dahlgren P, Dee D, Diamantakis M, Dragani R, Flemming J, Forbes R, Fuentes M, Geer A, Haimberger L, Healy S, Hogan RJ, Hólm E, Janisková M, Keeley S, Laloyaux P, Lopez P, Lupu C, Radnoti G, Rosnay P, Rozum I, Vamborg F, Villaume S, Thépaut (2020) J. N. The ERA5 global reanalysis. *Quarterly Journal of the Royal Meteorological Society*, 146(730), 1999–2049. <https://doi.org/10.1002/qj.3803>
26. Huang Z, Zhong L, Ma Y, Fu Y (2021) Development and evaluation of spectral nudging strategy for the simulation of summer precipitation over the Tibetan Plateau using WRF (v4.0). *Geosci Model Dev* 14(5):2827–2841. <https://doi.org/10.5194/gmd-14-2827-2021>
27. Iacono MJ, Delamere JS, Mlawer EJ, Shephard MW, Clough SA, Collins WD (2008) Radiative forcing by long-lived greenhouse gases: Calculations with the AER radiative transfer models. *J Phys Res* 113(D13). <https://doi.org/10.1029/2008jd009944>
28. Jacob D, Petersen J, Eggert B, Alias A, Christensen OB, Bouwer LM, Braun A, Colette A, Déqué M, Georgievski G (2014) EURO-CORDEX: new high-resolution climate change projections for European impact research. *Reg Environ Chang* 14(2):563–578. <https://doi.org/10.1007/s10113-013-0499-2>
29. Kang S, Xu Y, You Q, Flügel W-A, Pepin N, Yao T (2010) Review of climate and cryospheric change in the Tibetan Plateau. *Environmental research letters* 5(1). <https://doi.org/10.1088/1748-9326/5/1/015101>
30. Kattel DB, Yao T, Yang K, Tian L, Yang G, Joswiak D (2012) Temperature lapse rate in complex mountain terrain on the southern slope of the central Himalayas. *Theoret Appl Climatol* 113(3–

- 4):671–682. <https://doi.org/10.1007/s00704-012-0816-6>
31. Kendon E, Prein A, Senior C, Stirling A (2021) Challenges and outlook for convection-permitting climate modelling. *Philosophical Transactions of the Royal Society A* 379(2195):20190547. <https://doi.org/10.1098/rsta.2019.0547>
32. Kuang X, Jiao JJ (2016) Review on climate change on the Tibetan Plateau during the last half century. *Journal of Geophysical Research: Atmospheres* 121(8):3979–4007. <https://doi.org/10.1002/2015jd024728>
33. Kukulies J, Chen D, Wang M (2020) Temporal and spatial variations of convection, clouds and precipitation over the Tibetan Plateau from recent satellite observations. Part II: Precipitation climatology derived from global precipitation measurement mission. *Int J Climatol* 40(11):4858–4875. <https://doi.org/10.1002/joc.6493>
34. Li P, Furtado K, Zhou T, Chen H, Li J (2021) Convection-permitting modelling improves simulated precipitation over the central and eastern Tibetan Plateau. *Q J R Meteorol Soc* 147(734):341–362. <https://doi.org/10.1002/qj.3921>
35. Li P, Furtado K, Zhou T, Chen H, Li J, Guo Z, Xiao C (2020) The diurnal cycle of East Asian summer monsoon precipitation simulated by the Met Office Unified Model at convection-permitting scales. *Clim Dyn* 55(1):131–151. <https://doi.org/10.1007/s00382-018-4368-z>
36. Li X, Gao Y, Pan Y, Xu Y (2018) Evaluation of near-surface wind speed simulations over the Tibetan Plateau from three dynamical downscalings based on WRF model. *Theoret Appl Climatol* 134(3):1399–1411. <https://doi.org/10.1007/s00704-017-2353-9>
37. Liang X-Z (2004) Regional climate model simulation of summer precipitation diurnal cycle over the United States. *Geophys Res Lett* 31(24). <https://doi.org/10.1029/2004gl021054>
38. Lin C, Chen D, Yang K, Ou T (2018) Impact of model resolution on simulating the water vapor transport through the central Himalayas: implication for models' wet bias over the Tibetan Plateau. *Clim Dyn* 51(9–10):3195–3207. <https://doi.org/10.1007/s00382-018-4074-x>
39. Liu C, Ikeda K, Rasmussen R, Barlage M, Newman AJ, Prein AF, Chen F, Chen L, Clark M, Dai A (2017) Continental-scale convection-permitting modeling of the current and future climate of North America. *Clim Dyn* 49(1):71–95. <https://doi.org/10.1007/s00382-016-3327-9>
40. Lucas-Picher P, Argüeso D, Brisson E, Trambly Y, Berg P, Lemonsu A, Kotlarski S, Caillaud C (2021) Convection
41. -permitting modeling with regional climate models: Latest developments and next steps. *WIREs Climate Change*, 12(6). <https://doi.org/10.1002/wcc.731>
42. Lucas-Picher P, Wulff-Nielsen M, Christensen JH, Aðalgeirsdóttir G, Mottram R, Simonsen SB (2012) Very high resolution regional climate model simulations over Greenland: Identifying added value. *Journal of Geophysical Research: Atmospheres* 117(D2). <https://doi.org/10.1029/2011jd016267>
43. Maussion F, Scherer D, Finkelnburg R, Richters J, Yang W, Yao T (2011) WRF simulation of a precipitation event over the Tibetan Plateau, China – an assessment using remote sensing and

- ground observations. *Hydrol Earth Syst Sci* 15(6):1795–1817. <https://doi.org/10.5194/hess-15-1795-2011>
44. Miura H (2007) An Upwind-Biased Conservative Advection Scheme for Spherical Hexagonal–Pentagonal Grids. *Mon Weather Rev* 135(12):4038–4044. <https://doi.org/10.1175/2007mwr2101.1>
 45. Nakanishi M, Niino H (2006) An Improved Mellor–Yamada Level-3 Model: Its Numerical Stability and Application to a Regional Prediction of Advection Fog. *Boundary Layer Meteorol* 119(2):397–407. <https://doi.org/10.1007/s10546-005-9030-8>
 46. Niu G-Y, Yang Z-L, Mitchell KE, Chen F, Ek MB, Barlage M, Kumar A, Manning K, Niyogi D, Rosero E, Tewari M, Xia Y (2011) The community Noah land surface model with multiparameterization options (Noah-MP): 1. Model description and evaluation with local-scale measurements. *J Phys Res* 116(D12). <https://doi.org/10.1029/2010jd015139>
 47. Niu X, Tang J, Wang S, Fu C, Chen D (2020) On the sensitivity of seasonal and diurnal precipitation to cumulus parameterization over CORDEX-EA-II. *Clim Dyn* 54(1):373–393. <https://doi.org/10.1007/s00382-019-05010-w>
 48. Ou T, Chen D, Chen X, Lin C, Yang K, Lai H-W, Zhang F (2020) Simulation of summer precipitation diurnal cycles over the Tibetan Plateau at the gray-zone grid spacing for cumulus parameterization. *Clim Dyn* 54(7–8):3525–3539. <https://doi.org/10.1007/s00382-020-05181-x>
 49. Prein AF, Gobiet A, Suklitsch M, Truhetz H, Awan NK, Keuler K, Georgievski G (2013) Added value of convection permitting seasonal simulations. *Clim Dyn* 41(9–10):2655–2677. <https://doi.org/10.1007/s00382-013-1744-6>
 50. Prein AF, Langhans W, Fosser G, Ferrone A, Ban N, Goergen K, Keller M, Tolle M, Gutjahr O, Feser F, Brisson E, Kollet S, Schmidli J, van Lipzig NP, Leung R (2015) Jun). A review on regional convection-permitting climate modeling: Demonstrations, prospects, and challenges. *Rev Geophys* 53(2):323–361. <https://doi.org/10.1002/2014RG000475>
 51. Prein AF, Rasmussen R, Castro CL, Dai A, Minder J (2020) Special issue: Advances in convection-permitting climate modeling. *Clim Dyn* 55(1–2):1–2. <https://doi.org/10.1007/s00382-020-05240-3>
 52. Prein AF, Rasmussen R, Stephens G (2017) Challenges and advances in convection-permitting climate modeling. *Bull Am Meteorol Soc* 98(5):1027–1030. <https://doi.org/10.1175/BAMS-D-16-0263.1>
 53. Qiu J (2008) China: the third pole. *Nature News* 454(7203):393–396. <https://doi.org/10.1038/454393a>
 54. Rasmussen R, Ikeda K, Liu C, Gochis D, Clark M, Dai A, Gutmann E, Dudhia J, Chen F, Barlage M (2014) Climate change impacts on the water balance of the Colorado headwaters: High-resolution regional climate model simulations. *J Hydrometeorol* 15(3):1091–1116. <https://doi.org/10.1175/jhm-d-13-0118.1>
 55. Rutan DA, Kato S, Doelling DR, Rose FG, Nguyen LT, Caldwell TE, Loeb NG (2015) CERES synoptic product: Methodology and validation of surface radiant flux. *J Atmos Ocean Technol* 32(6):1121–1143

56. Satoh M, Tomita H, Yashiro H, Miura H, Kodama C, Seiki T, Noda AT, Yamada Y, Goto D, Sawada M (2014) The non-hydrostatic icosahedral atmospheric model: Description and development. *Progress in Earth and Planetary Science* 1(1):1–32. <https://doi.org/10.1186/s40645-014-0018-1>
57. Schär C, Fuhrer O, Arteaga A, Ban N, Charpilloz C, Di Girolamo S, Hentgen L, Hoefler T, Lapillonne X, Leutwyler D, Osterried K, Panosetti D, Rüdüsühli S, Schlemmer L, Schulthess TC, Sprenger M, Ubbiali S, Wernli H (2020) Kilometer-Scale Climate Models: Prospects and Challenges. *Bull Am Meteorol Soc* 101(5):E567–E587. <https://doi.org/10.1175/bams-d-18-0167.1>
58. Schlemmer L, Hohenegger C, Schmidli J, Bretherton CS, Schär C (2011) An Idealized Cloud-Resolving Framework for the Study of Midlatitude Diurnal Convection over Land. *J Atmos Sci* 68(5):1041–1057. <https://doi.org/10.1175/2010jas3640.1>
59. Schwitalla T, Warrach-Sagi K, Wulfmeyer V, Resch M (2020) Near-global-scale high-resolution seasonal simulations with WRF-Noah-MP v.3.8.1. *Geosci Model Dev* 13(4):1959–1974. <https://doi.org/10.5194/gmd-13-1959-2020>
60. Skamarock WC, Klemp JB, Dudhia J, Gill DO, Liu Z, Berner J, Wang W, Powers JG, Duda MG, Barker DM (2019) A description of the advanced research WRF model version 4. *National Center for Atmospheric Research: Boulder, CO, USA*, 145
61. Sun X, Xue M, Brotzge J, McPherson RA, Hu X-M, Yang X-Q (2016) An evaluation of dynamical downscaling of Central Plains summer precipitation using a WRF-based regional climate model at a convection-permitting 4 km resolution. *Journal of Geophysical Research: Atmospheres* 121(23) 13,801-813,825. <https://doi.org/10.1002/2016jd024796>
62. Tang J, Song S, Wu J (2010) Impacts of the spectral nudging technique on simulation of the East Asian summer monsoon. *Theoret Appl Climatol* 101(1):41–51. <https://doi.org/10.1007/s00704-009-0202-1>
63. Tang J, Wang S, Niu X, Hui P, Zong P, Wang X (2017) Impact of spectral nudging on regional climate simulation over CORDEX East Asia using WRF. *Clim Dyn* 48(7–8):2339–2357. <https://doi.org/10.1007/s00382-016-3208-2>
64. Taraphdar S, Pauluis OM, Xue L, Liu C, Rasmussen R, Ajayamohan RS, Tessendorf S, Jing X, Chen S, Grabowski WW (2021) WRF Gray-Zone Simulations of Precipitation Over the Middle-East and the UAE: Impacts of Physical Parameterizations and Resolution. *Journal of Geophysical Research: Atmospheres* 126(10). <https://doi.org/10.1029/2021jd034648>
65. Taylor KE (2001) Summarizing multiple aspects of model performance in a single diagram. *Journal of Geophysical Research: Atmospheres* 106(D7):7183–7192. <https://doi.org/10.1029/2000jd900719>
66. Thompson, G., Field, P. R., Rasmussen, R. M., & Hall, W. D. (2008). Explicit forecasts of winter precipitation using an improved bulk microphysics scheme. Part II: Implementation of a new snow parameterization. *Monthly Weather Review*, 136(12), 5095-5115. <https://doi.org/10.1175/2008mwr2387.1>
67. von Storch, H., Langenberg, H., & Feser, F. (2000). A spectral nudging technique for dynamical downscaling purposes. *Monthly Weather Review*, 128(10), 3664-3673. <https://doi.org/10.1175/1520->

0493(2000)128<3664:ASNTFD>2.0.CO;2

68. Wang G, Wang T, Xue H (2021) Validation and comparison of surface shortwave and longwave radiation products over the three poles. *Int J Appl Earth Obs Geoinf* 104. <https://doi.org/10.1016/j.jag.2021.102538>
69. Wang X, Chen D, Pang G, Anwar SA, Ou T, Yang M (2021) Effects of cumulus parameterization and land-surface hydrology schemes on Tibetan Plateau climate simulation during the wet season: insights from the RegCM4 model. *Clim Dyn*. <https://doi.org/10.1007/s00382-021-05781-1>
70. Wang X, Tolksdorf V, Otto M, Scherer D (2020) WRF-based dynamical downscaling of ERA5 reanalysis data for High Mountain Asia: Towards a new version of the High Asia Refined analysis. *International Journal of Climatology*, 41(1),743–762. <https://doi.org/10.1002/joc.6686>
71. Wang Y, Wang L, Li X, Chen D (2018) Temporal and spatial changes in estimated near-surface air temperature lapse rates on Tibetan Plateau. *Int J Climatol* 38(7):2907–2921. <https://doi.org/10.1002/joc.5471>
72. Wu G, Liu Y, Zhang Q, Duan A, Wang T, Wan R, Liu X, Li W, Wang Z, Liang X (2007) The influence of mechanical and thermal forcing by the Tibetan Plateau on Asian climate. *J Hydrometeorol* 8(4):770–789. <https://doi.org/10.1175/jhm609.1>
73. XIAO L, GAO Y, CHEN F, XU J, LI K, LI X, JIANG Y (2016) Dynamic downscaling simulation of extreme temperature indices over the Qinghai-Xizang plateau. *Plateau Meteorology* 35(3):574–589. <https://doi.org/10.7522/j.issn.1000-0534.2016.00039>
74. Xu J, Koldunov N, Remedio ARC, Sein DV, Zhi X, Jiang X, Xu M, Zhu X, Fraedrich K, Jacob D (2018) On the role of horizontal resolution over the Tibetan Plateau in the REMO regional climate model. *Clim Dyn* 51(11–12):4525–4542. <https://doi.org/10.1007/s00382-018-4085-7>
75. Xu ZX, Gong TL, Li JY (2008) Decadal trend of climate in the Tibetan Plateau—regional temperature and precipitation. *Hydrol Process* 22(16):3056–3065. <https://doi.org/10.1002/hyp.6892>
76. Yao T, Xue Y, Chen D, Chen F, Thompson L, Cui P, Koike T, Lau WKM, Lettenmaier D, Mosbrugger V, Zhang R, Xu B, Dozier J, Gillespie T, Gu Y, Kang S, Piao S, Sugimoto S, Ueno K, Wang L, Wang W, Zhang F, Sheng Y, Guo W, Ailikun, Yang X, Ma Y, Shen SSP, Su Z, Chen F, Liang S, Liu Y, Singh VP, Yang K, Yang D, Zhao X, Qian Y, Zhang Y, Li Q (2019) Recent Third Pole's Rapid Warming Accompanies Cryospheric Melt and Water Cycle Intensification and Interactions between Monsoon and Environment: Multidisciplinary Approach with Observations, Modeling, and Analysis. *Bull Am Meteorol Soc* 100(3):423–444. <https://doi.org/10.1175/bams-d-17-0057.1>
77. Yeh T-C (1957) The wind structure and heat balance in the lower troposphere over the Tibetan Plateau and its surroundings. *Acta Meteor Sinica* 28:108–121
78. Yun Y, Liu C, Luo Y, Liang X, Huang L, Chen F, Rasmussen R (2020) Convection-permitting regional climate simulation of warm-season precipitation over Eastern China. *Clim Dyn* 54(3):1469–1489. <https://doi.org/10.1007/s00382-019-05070-y>
79. Zhang Y, Chen H (2016) Comparing CAM5 and Superparameterized CAM5 Simulations of Summer Precipitation Characteristics over Continental East Asia: Mean State, Frequency–Intensity

Relationship, Diurnal Cycle, and Influencing Factors. *J Clim* 29(3):1067–1089.

<https://doi.org/10.1175/jcli-d-15-0342.1>

80. Zhou X, Yang K, Ouyang L, Wang Y, Jiang Y, Li X, Chen D, Prein A (2021) Added value of kilometer-scale modeling over the third pole region: a CORDEX-CPTP pilot study. *Clim Dyn*.
<https://doi.org/10.1007/s00382-021-05653-8>
81. Zhu L, Huang G, Fan G, Qu X, Zhao G, Hua W (2017) Evolution of surface sensible heat over the Tibetan Plateau under the recent global warming hiatus. *Adv Atmos Sci* 34(10):1249–1262.
<https://doi.org/10.1007/s00376-017-6298-9>
82. Yun, Y., Liu, C., Luo, Y., Liang, X., Huang, L., Chen, F., & Rasmussen, R. (2020). Convection-permitting regional climate simulation of warm-season precipitation over Eastern China. *Climate Dynamics*, 54(3), 1469-1489. <https://doi.org/10.1007/s00382-019-05070-y>
83. Zhang, Y., & Chen, H. (2016). Comparing CAM5 and Superparameterized CAM5 Simulations of Summer Precipitation Characteristics over Continental East Asia: Mean State, Frequency–Intensity Relationship, Diurnal Cycle, and Influencing Factors. *Journal of Climate*, 29(3), 1067-1089.
<https://doi.org/10.1175/jcli-d-15-0342.1>
84. Zhou, X., Yang, K., Ouyang, L., Wang, Y., Jiang, Y., Li, X., Chen, D., & Prein, A. (2021). Added value of kilometer-scale modeling over the third pole region: a CORDEX-CPTP pilot study. *Climate Dynamics*.
<https://doi.org/10.1007/s00382-021-05653-8>
85. Zhu, L., Huang, G., Fan, G., Qu, X., Zhao, G., & Hua, W. (2017). Evolution of surface sensible heat over the Tibetan Plateau under the recent global warming hiatus. *Advances in Atmospheric Sciences*, 34(10), 1249-1262. <https://doi.org/10.1007/s00376-017-6298-9>

Figures

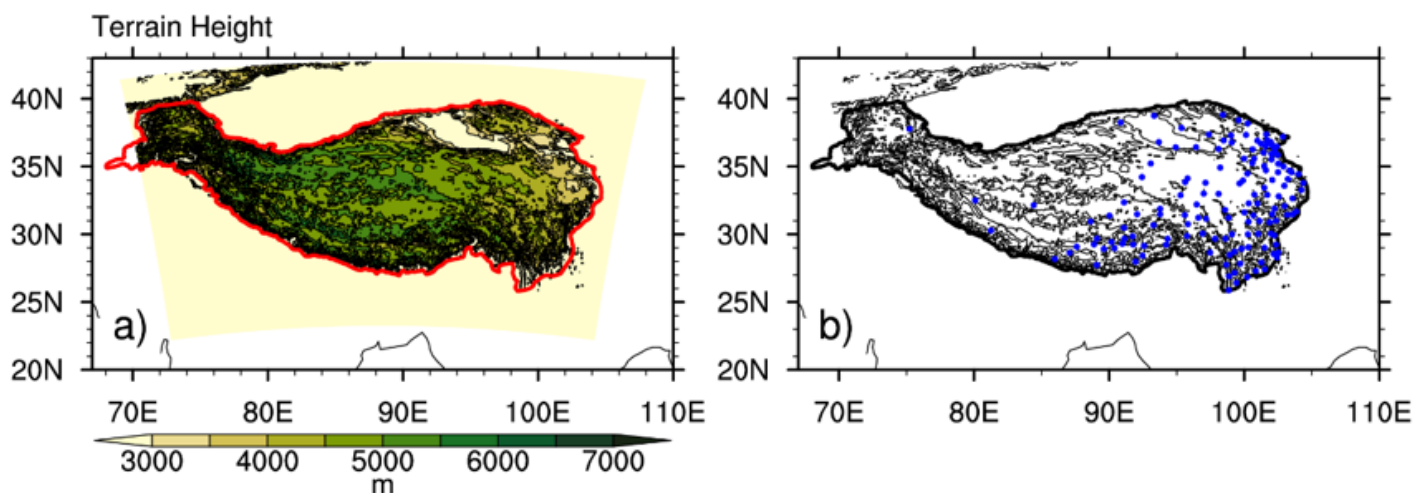


Figure 1

The simulation domain (yellow shading) with the TP framed with red lines (a), and the locations of the meteorological stations over the TP (b)

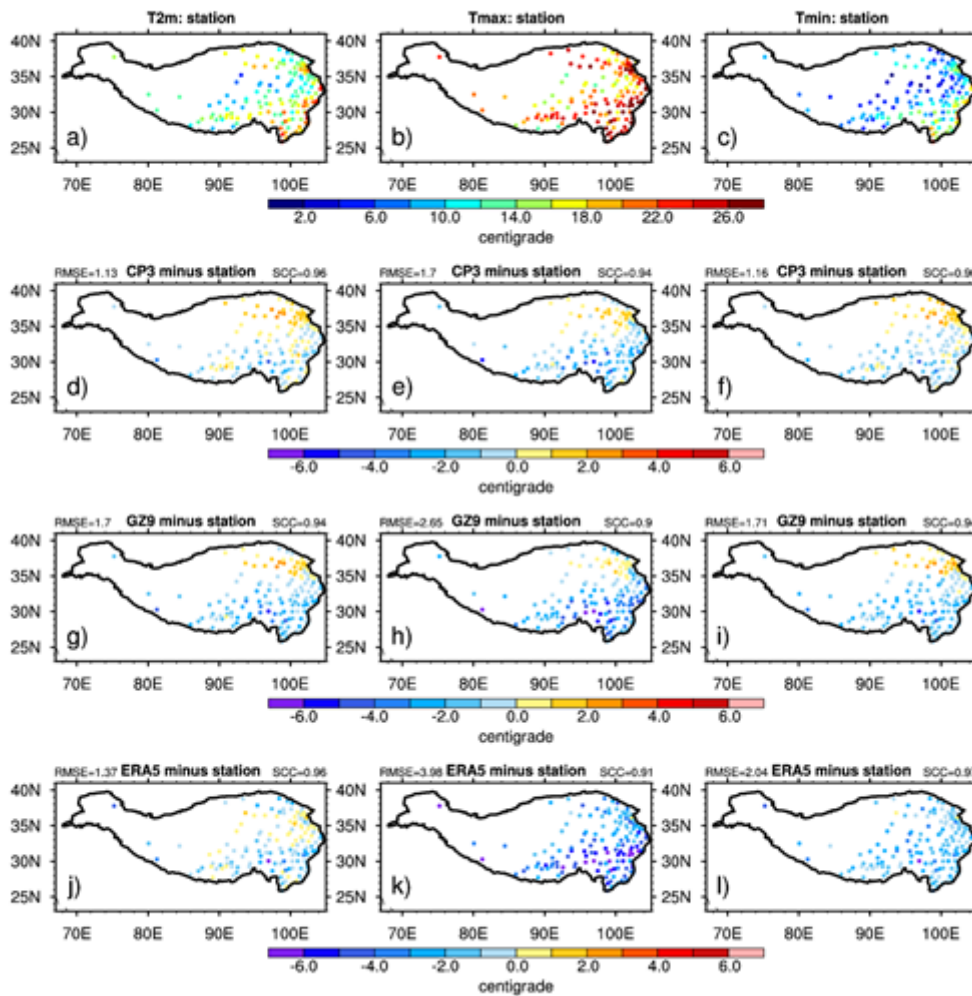


Figure 2

The 10-year averaged (2009-2018) summer mean T2m, Tmax, and Tmin from the in-situ observations (a, b, c), the biases in GZ9 (d, e, f), the bias in CP3 (g, h, i), and the bias in ERA5 (j, k, l)

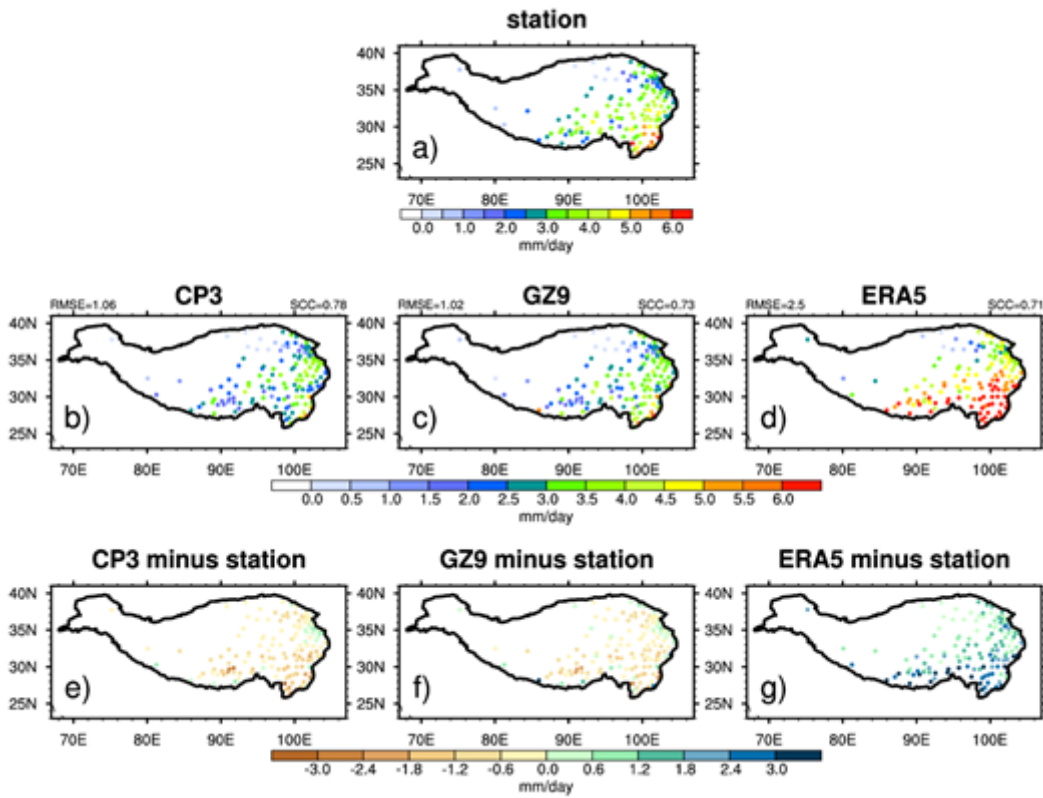


Figure 3

The first row: 10-year averaged summer precipitation from the station observations (a); the second row: 10-year averaged summer precipitation from CP3 (b), GZ9 (c) and ERA5 (d); the third row: the bias of CP3 (e), GZ9(f) and ERA5 (g)

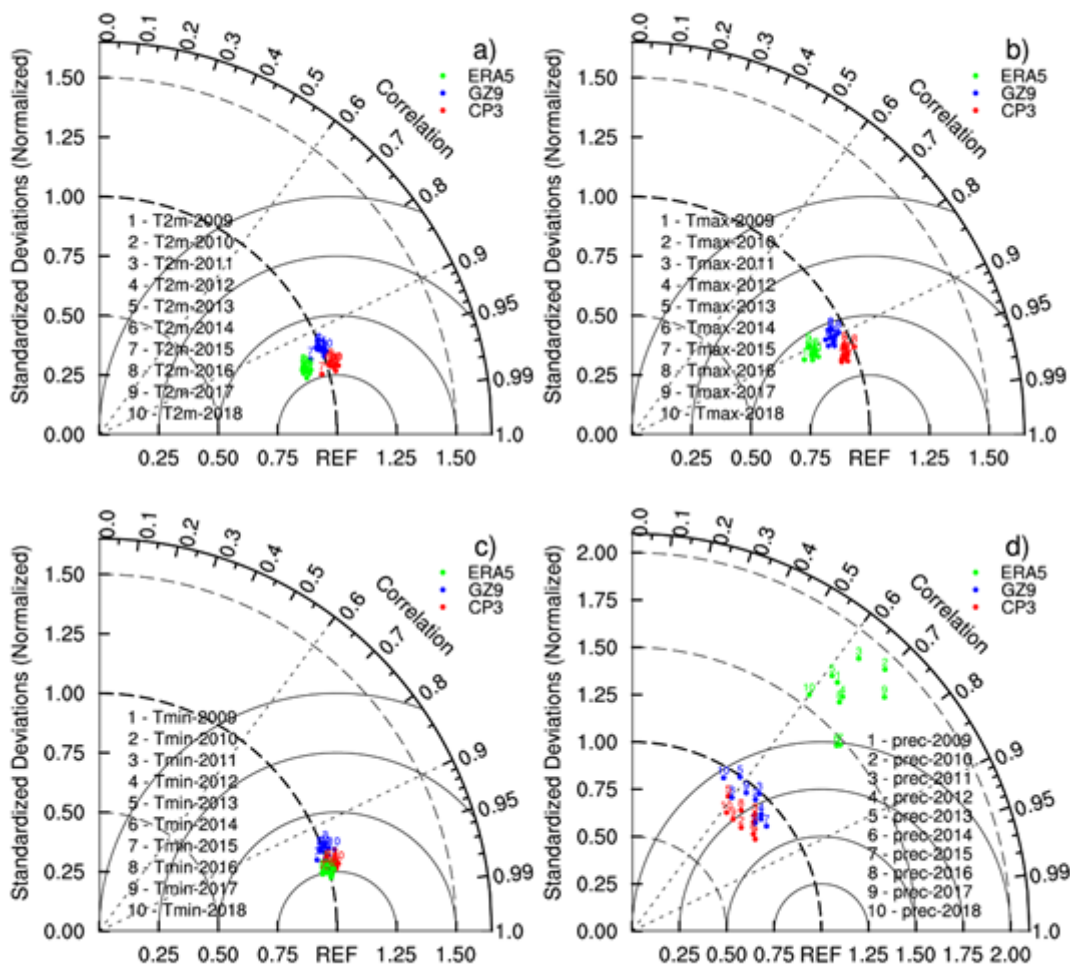


Figure 4

Taylor diagrams for WRF simulated and ERA5-derived summer T2m (a), Tmax (b), Tmin (c) and precipitation (d) compared with station observations from 2009 to 2018

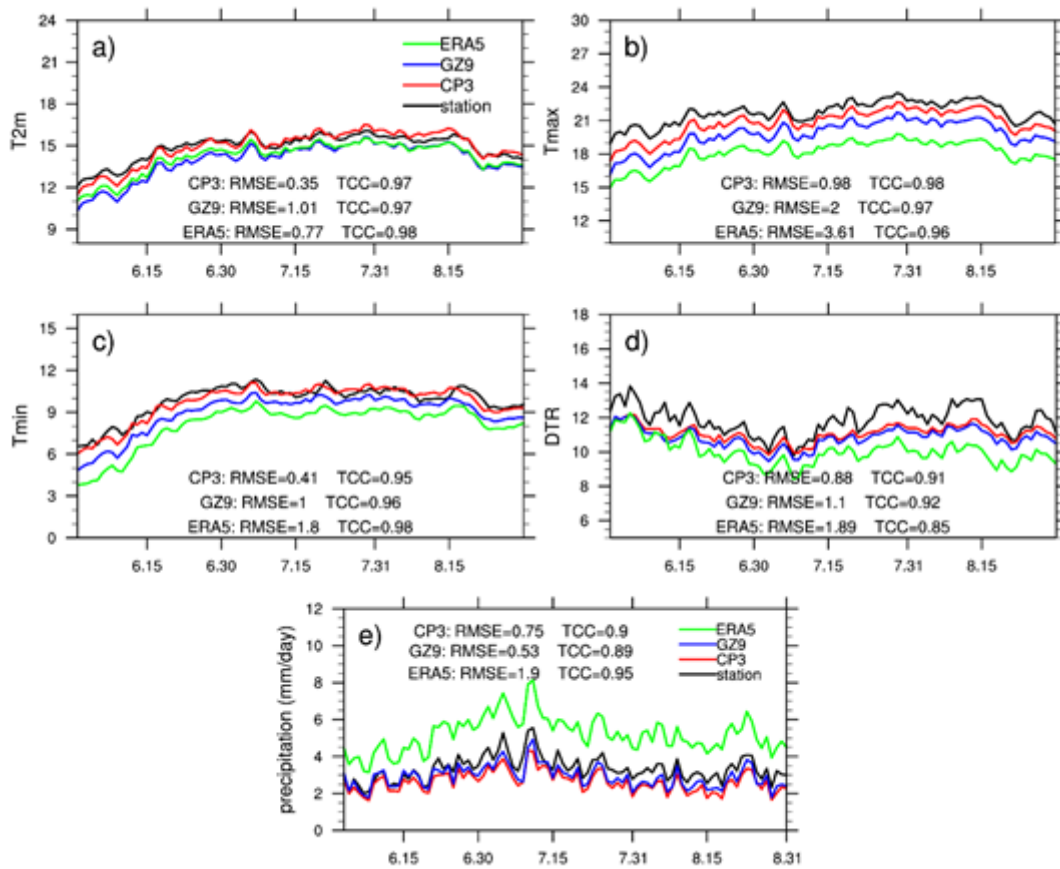


Figure 5

10-year averaged daily variations of regional mean T2m (a), Tmax (b), Tmin (c), DTR (d) and precipitation (from the in-situ observations and the simulations of CP3 and GZ9)

Figure 6

The spatial distributions of TCCs for the simulated summer T2m, Tmax, and Tmin in CP3 (a, b, c), GZ9 (d, e, f) and ERA5 (g, h, i)

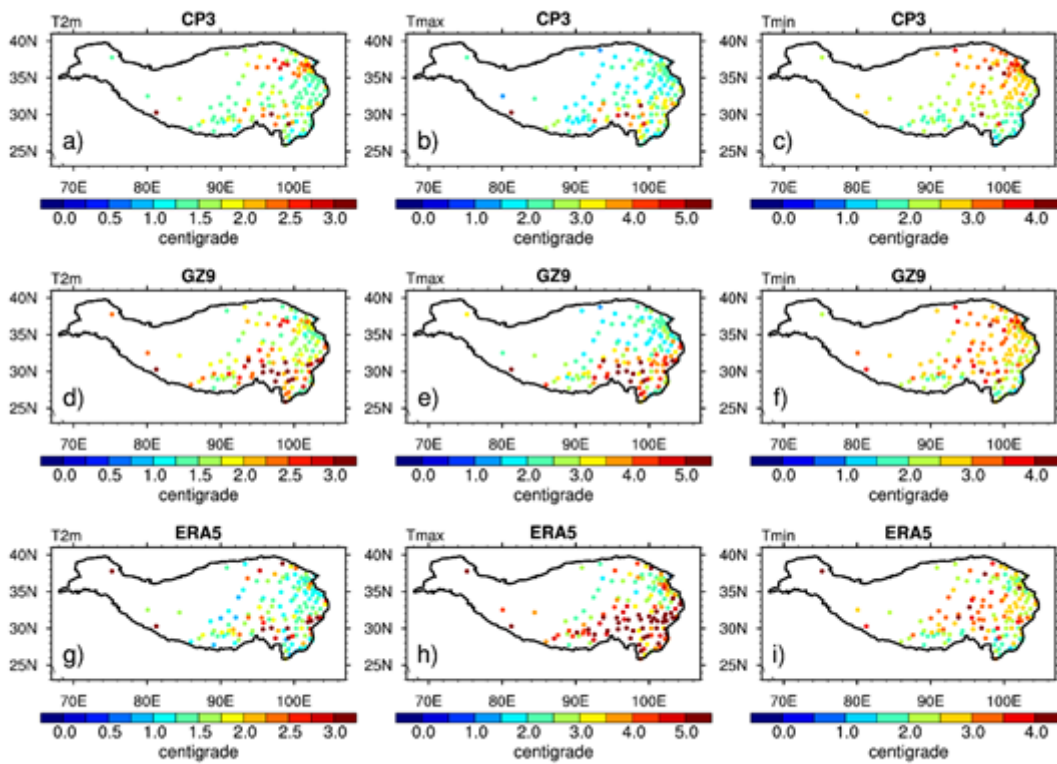


Figure 7

Similar to Fig. 6, but for RMSEs

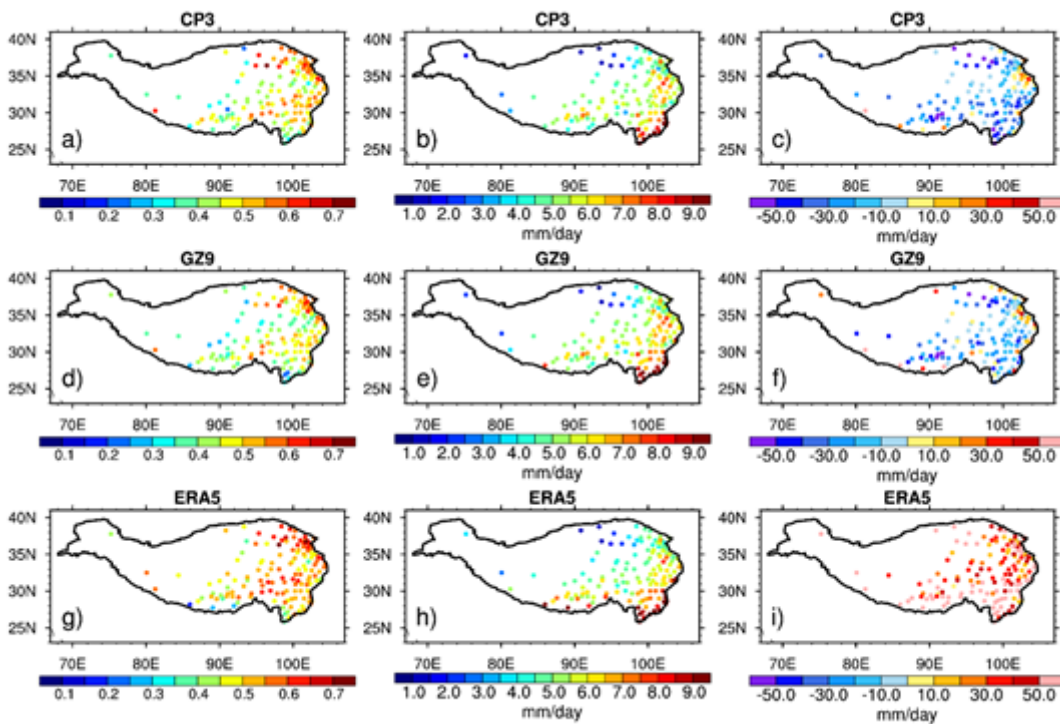


Figure 8

The spatial distribution of TCCs (the first column), RMSEs (the second column) and RBs (the third column) of precipitation in GZ9, CP3 and ERA

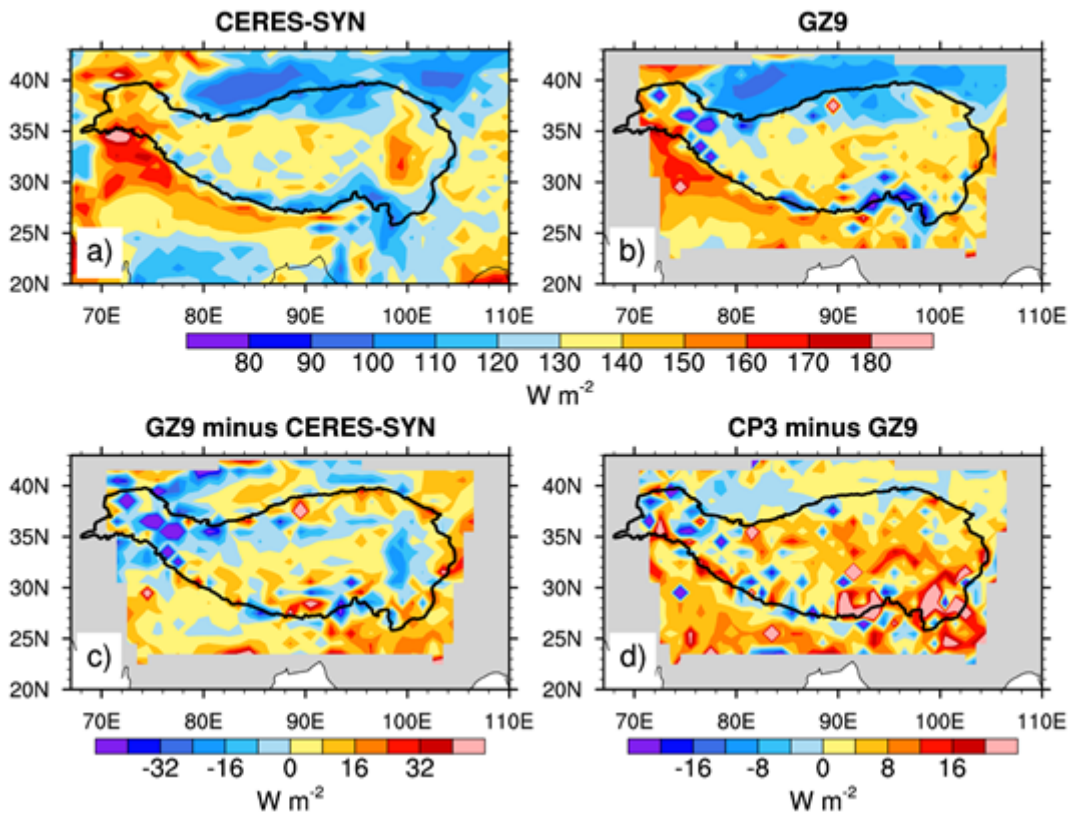


Figure 9

the 10-yr averaged net radiation (net shortwave radiation and net longwave radiation) at surface from CERES-SYN, GZ9, the difference between GZ9 and CERES-SYN, as well as the difference between GZ9 and CP3

Figure 10

Similar to Fig. 9, but for cloud cover at 500-300hPa

Figure 11

Similar to Fig. 9, but for cloud cover above 300hPa

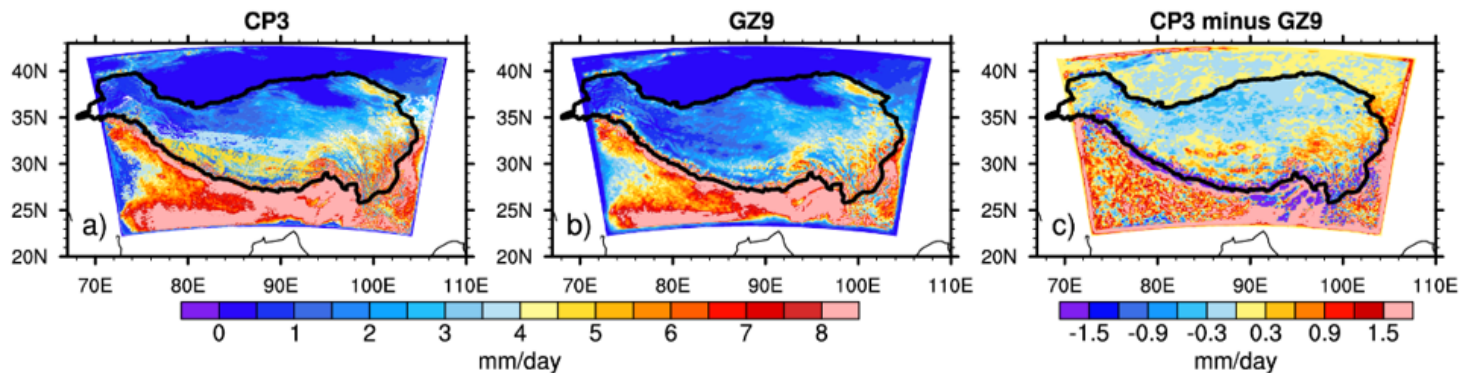


Figure 12

Simulated precipitation in CP3, GZ9 and the difference between them

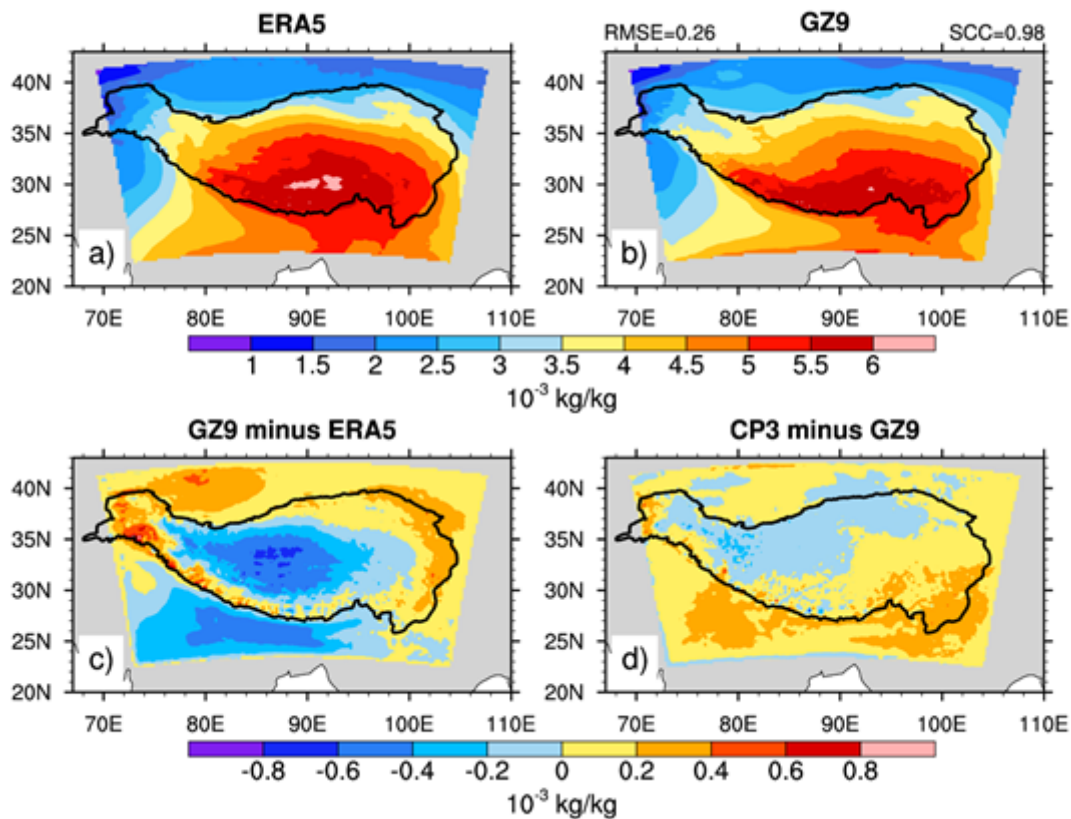


Figure 13

The specific humidity at 500hPa in ERA5, GZ9, the difference between GZ9 and ERA5 and the difference between CP3 and GZ9

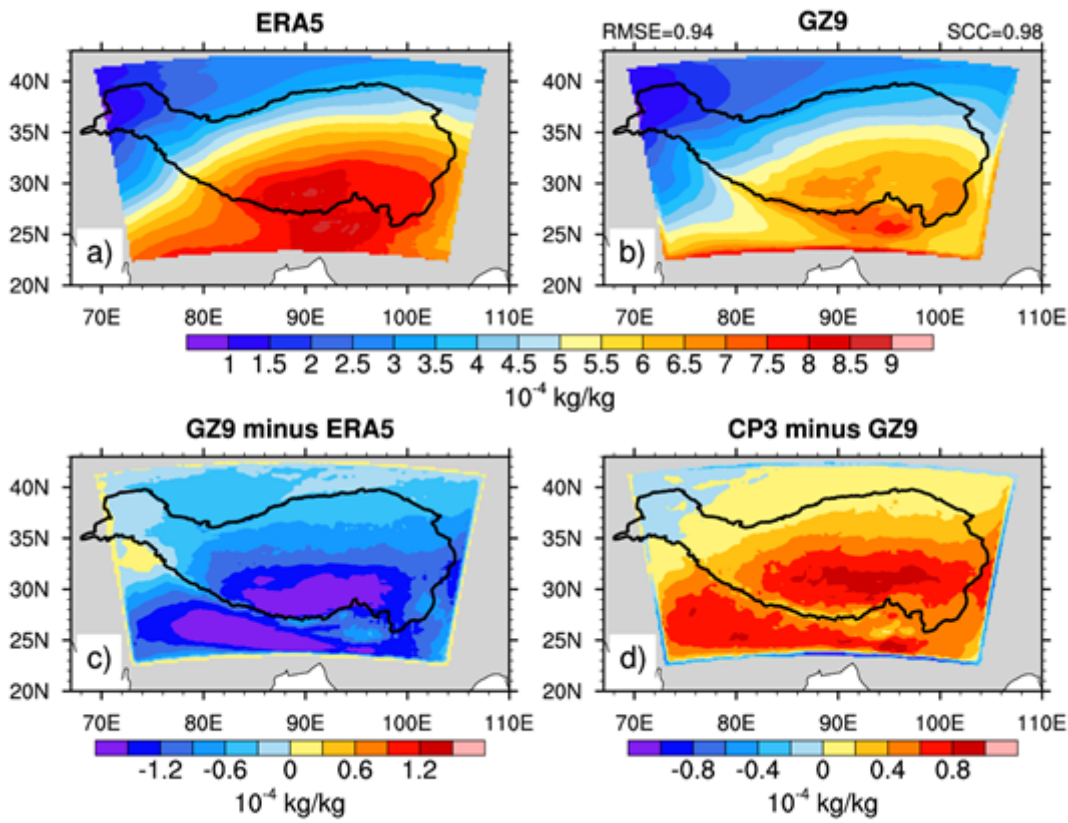


Figure 14

Similar to Fig. 13, but at 300hPa

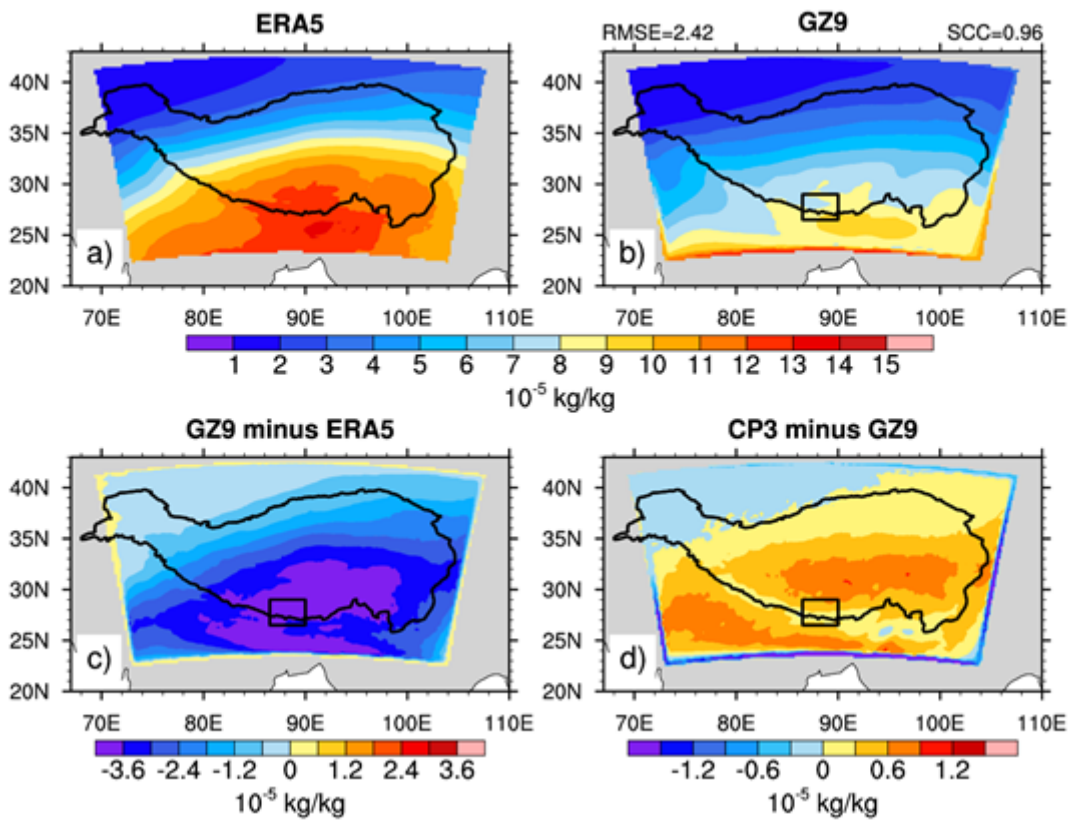


Figure 15

Similar to Fig. 13, but at 200hPa

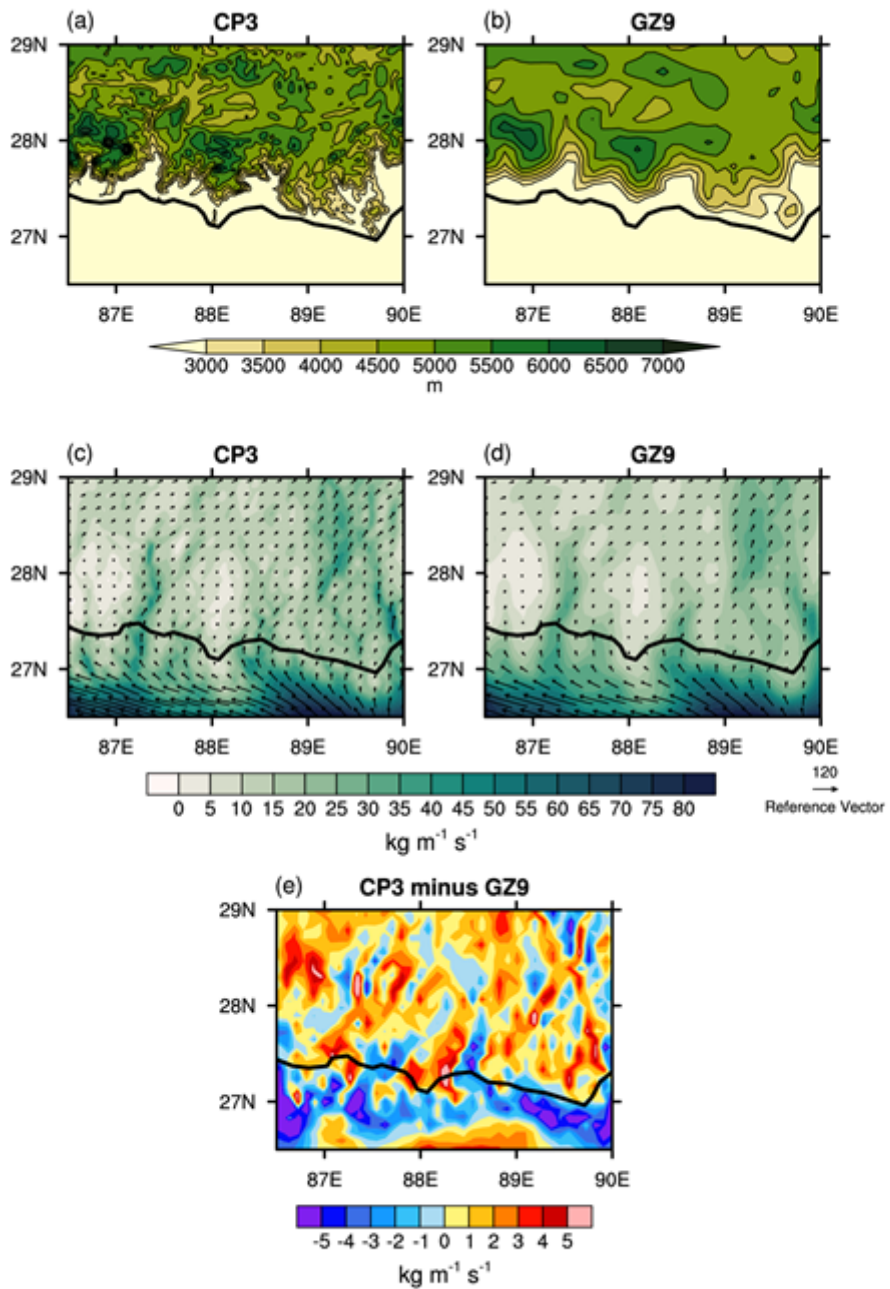


Figure 16

The first row: topography of the target region which is framed with black lines in Fig. 15; the second row: spatial pattern of total column water vapor transport (vector) and its v component (color) in CP3 and GZ9; the third row: the difference of the v component of total column water vapor transport between CP3 and GZ9